Correspondence to:
B. Niu,
b.niu@imperial.ac.uk

The impact of reservoir conditions on the residual trapping of carbon dioxide in Berea sandstone

Ben Niu[1,2,3], Ali Al-Menhali[1,3], and Samuel C. Krevor[1,3]

[1]Department of Earth Science and Engineering, Imperial College, London, UK, [2]Department of Chemical Engineering, Imperial College, London, UK, [3]Qatar Carbonates and Carbon Storage Research Centre, Imperial College, London, UK

Abstract The storage of carbon dioxide in deep brine-filled permeable rocks is an important tool for CO_2 emissions mitigation on industrial scales. Residual trapping of CO_2 through capillary forces within the pore space of the reservoir is one of the most significant mechanisms for storage security and is also a factor determining the ultimate extent of CO_2 migration within the reservoir. In this study we have evaluated the impact of reservoir conditions of pressure, temperature, and brine salinity on the residual trapping characteristic curve of a fired Berea sandstone rock. The observations demonstrate that the initial-residual characteristic trapping curve is invariant across a wide range of pressure, temperature, and brine salinities and is also the same for CO_2-brine systems as a N_2-water system. The observations were made using a reservoir condition core-flooding laboratory that included high-precision pumps, temperature control, the ability to recirculate fluids for weeks at a time, and an X-ray CT scanner. Experimental conditions covered pressures of 5–20 MPa, temperatures of 25–50°C, and 0–5 mol/kg NaCl brine salinity. A novel coreflooding approach was developed, making use of the capillary end effect to create a large range in initial CO_2 saturation (0.15–0.6) in a single coreflood. Upon subsequent flooding with CO_2-equilibriated brine, the observation of residual saturation corresponded to the wide range of initial saturations before flooding resulting in a rapid construction of the initial-residual curve. For each condition we report the initial-residual curve and the resulting parameterization of the *Land* hysteresis models.

1. Introduction

The residual trapping of CO_2 in the deep subsurface is a key process for maximizing capacity and ensuring the integrity of CO_2 sequestration at industrial scales. The most recent official CO_2 storage capacity estimate for the United States in *Warwick et al.* [2013] considers 90% of the total available capacity to be associated with residual trapping and capacity estimates for other countries show similar sensitivity to the character of residual trapping [*Gammer et al.*, 2011; *Halland et al.*, 2011]. The extent of trapping and its relationship to flow property hysteresis has an important impact on the movement of the mobile sections of a subsurface CO_2 plume, as shown by a number of studies [*Juanes et al.*, 2006; *Doughty*, 2007; *Hesse et al.*, 2008]. Going further, *Qi et al.* [2009] showed that flow property hysteresis could even be used to design reservoir management strategies that lead to significantly enhanced trapping.

Residual trapping has been investigated extensively for petroleum engineering applications for two primary reasons. Intuitively, residual trapping has a primary control on the ultimate oil recovery in conventional production processes. Where water is being used to drive oil from a reservoir, for example, a product of the sweep, the total fraction of the reservoir contacted by the injected water, and the complement of the residually trapped oil saturation determines the ultimate recovery [*Lake*, 1989]. This is the analog to the role of residual trapping in capacity estimation for CO_2 storage. The product of the spatial extent of the CO_2 plume and residually trapped saturation will determine the extent to which residual trapping contributes to the total storage capacity of a reservoir [*Warwick et al.*, 2013; *Gammer et al.*, 2011; *Halland et al.*, 2011].

Second, but at least as important, is that since the work of *Naar and Henderson* [1961] and *Land* [1968] the most widely used continuum approaches for modeling multiphase flow in strongly water wet systems have assumed that residual trapping can be used to parameterize models for hysteresis in relative permeability and capillary pressure constitutive functions. In this approach, the nonwetting phase saturation, S_{nw}, is conceptualized as consisting of parts that are *connected*, $S_{nw,c}$, or contributing to flow and parts that are

disconnected, $S_{nw,d}$, or not contributing to flow, $S_{nw} = S_{nw,c} + S_{nw,d}$ and $S_{nw,c} \leq S_{nw}$. It is assumed that relative permeability to the nonwetting phase, $k_{r,nw}$, is a function only of the connected saturation. Along a bounding drainage curve all of the nonwetting phase is assumed to be connected, $S_{nw} = S_{nw,c}$, whereas on an imbibition curve the connected saturation must be calculated from a model that uses observations of residual trapping for its parameterization. A number of models have been developed around this concept. Reviews included in *Pentland et al*. [2010] and *Joekar-Niasar et al*. [2013] discuss the models developed by *Land* [1968], *Lenhard and Parker* [1987], *Ma and Youngren* [1994], *Jerauld* [1997], *Kleppe et al*. [1997], and *Spiteri et al*. [2008]. In summary, models for hysteresis consist of (i) a relationship between the permeability of the nonwetting phase and its connected or flowing saturation, (ii) a model for the connected saturation as a function of saturation history and residual trapping characteristic, and (iii) a model for the residual trapping characteristic, relating the residual trapping saturation of the nonwetting phase to the maximum saturation obtained before imbibition. This third component concerning the residual trapping is the only observation-based input into the parameterization of hysteresis (Imbibition bounding or scanning curves can generally be used interchangeably with observations of residual trapping to constrain these models but there is an implied self-consistency. Specified imbibition curves imply an *IR* relationship and vice versa. A notable variation is the widely used model of *Killough* [1976] which includes extra parameters to allow for the tuning of the curvature of the scanning curves between the bounding drainage and residual trapping points. This can obviously only be obtained from observations of the scanning curves themselves.).

For illustrative purposes we make use of one of the earliest and simpler iterations of this approach, suggested by *Land* [1968] and employed for modeling CO_2 storage in *Kumar et al*. [2005] and *Qi et al*. [2009]. In this version $k^i_{r,CO_2}(S_{CO_2})$, the imbibition relative permeability to CO_2 at a given saturation is set as equivalent to the drainage relative permeability function, k^d_{r,CO_2}, evaluated at the connected saturation

$$k^i_{r,CO_2}(S_{CO_2}) = k^d_{r,CO_2}(S_{CO_2,c}). \tag{1}$$

The connected saturation can be obtained by the model proposed in *Land* [1968] reproduced here

$$S^*_{CO_2,c} = \frac{1}{2}\left[(S^*_{CO_2} - S^*_{CO_2,r}) + \sqrt{(S^*_{CO_2} - S^*_{CO_2,r})^2 + \frac{4}{C}(S^*_{CO_2} - S^*_{CO_2,r})}\right]. \tag{2}$$

Where $S^*_{CO_2} = S_{CO_2}/(1 - S_{w,irr})$ is the saturation normalised to the irreducible water saturation. In this work the irreducible water saturation was not available and the data is reported unnormalised. The parameter C is found by fitting a curve to a plot of the residual saturation, $S_{CO_2,r}$, versus the initial saturation prior to imbibition, $S_{CO_2,i}$. The models used to generate the fitting curve are empirical relationship, e.g., the model proposed in *Land* [1968] is given by

$$S_{CO_2,r} = \frac{S_{CO_2,i}}{1 + CS_{CO_2,i}}. \tag{3}$$

The *IR* curves for various values of C and the corresponding imbibition scanning curves are shown in Figure 1.

Like the other constitutive relationships describing multiphase flow, capillary pressure, and relative permeability, the *IR* characteristic of a rock is considered to be invariant across a wide range of fluid pairs and conditions of temperature, pressure, and brine salinity so long as the wetting state of the system is similar between systems. It is well known that the properties will vary, however, if these conditions control the wetting state of the system [*Salathiel*, 1973; *Wang*, 1988] or the flow velocity v, viscosity μ, and interfacial tension σ combine in a way such that the dimensionless capillary number, $N_c = v\mu/\sigma$, exceeds a critical value for desaturation. For Berea sandstone this has been observed to be in the range $N_c > 10^{-5} - 10^{-4}$ [*Taber*, 1969; *Foster*, 1973; *Gupta and Trushenski*, 1979].

Recent observations, however, have raised doubts about whether these general observations extend to the CO_2-brine system. Resolving this uncertainty and its potential impact on residual trapping was the focus of this work. In particular, observations of contact angles of CO_2-brine systems on polished mineral surfaces reported by *Chiquet et al*. [2007], *Espinoza and Santamarina* [2010], *Broseta et al*. [2012], and *Jung and Wan* [2012] suggested that the wetting properties of the CO_2-brine-rock system may be sensitive to the pressure, temperature, and brine salinity of the system. This would imply that the multiphase flow properties themselves could be dependent on reservoir conditions. Preliminary observations consistent with an effect of
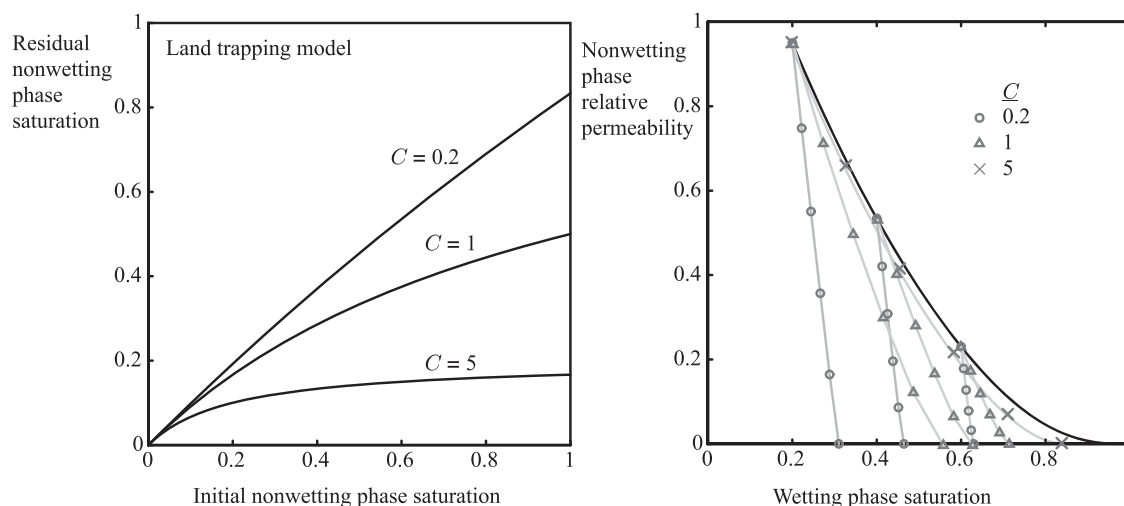
Figure 1. The graph on the left shows *IR* characteristic residual trapping curves using the model of *Land* [1968] for various values of the constant *C*. On the right imbibition curves departing from the primary drainage curve are shown for the different values of *C*. As the value of the constant increases, trapping decreases and hysteresis in the relative permeability necessarily weakens.

reservoir conditions or fluid properties on the relative permeability have been reported by *Bachu and Bennion* [2008] and *Berg et al.* [2013] and on residual trapping by *Pentland et al.* [2011] and *El-Maghraby and Blunt* [2012]. A dependence of multiphase flow properties on reservoir conditions for the CO_2-brine system would have major implications for the evaluation of CO_2 storage resources, the management of storage projects, and the capacity for a particular reservoir to secure CO_2 in a residually trapped form.

A number of observations of the residual trapping characteristics of CO_2-brine-rock systems have been reported in the last 5 years. These studies were performed to obtain the trapping characteristics at a real or nominally representative reservoir conditions and they are not sufficient on their own or as a compiled data set for an evaluation of the influence of the reservoir condition on trapping. An early observation of residual trapping was provided by *Suekane et al.* [2008] and the first characterization of the *IR* curve with supercritical CO_2 in a consolidated rock was reported by *Pentland et al.* [2011]. In this work less trapping was observed for a CO_2-brine system in Berea sandstone compared with a decane-brine pair, consistent with a less strongly wetting system for CO_2-brine. More characteristic trapping curves have been subsequently published for Berea sandstone [*Krevor et al.*, 2012; *Akbarabadi and Piri*, 2013], other sandstones including rocks from pilot CO_2 storage sites in the United States and Australia [*Krevor et al.*, 2012] and carbonate rocks [*El-Maghraby and Blunt*, 2012; *Bachu*, 2013], but most of these do not compare results between various conditions or fluid pairs. Pore-scale observations of residually trapped CO_2 at reservoir conditions have also been made by *Silin et al.* [2011] in a synchrotron and by *Iglauer et al.* [2011] and *Andrew et al.* [2014] using bench-scale micro CT. The observed bubble morphology in these works suggests both sandstone and carbonate rocks to be water wetting in the presence of CO_2. Despite this abundance of high-quality data, meta-analyses of the results in this literature reported in *Bachu* [2013] and *Burnside and Naylor* [2014] demonstrate the inadequacy of the compiled data set for assessing the impact of reservoir conditions on residual trapping or other multiphase flow properties. Resolving the uncertainty was the focus of this work.

We report an analysis of the impact of reservoir conditions on residual trapping in fired Berea sandstone using a group of experimental observations deriving the residual trapping characteristic curves in CO_2-brine systems in which pressure, temperature, and brine salinity were systematically varied across seven tests. For comparison with a system known to be strongly water wet an experiment was also performed with N_2 and water. Conditions were varied to cover a range representative of subsurface conditions in real target storage reservoirs and with the CO_2-rich phase existing as a gaseous, low-density supercritical fluid and high-density supercritical fluid. A novel coreflooding technique was developed and used, combining the deliberate creation of capillary pressure gradients in the core with in situ saturation monitoring to rapidly construct the initial-residual curve. An initial version of the technique was presented in *Krevor et al.* [2012] and further development presented here included the use of reservoir simulation to aid in the design of the test parameters, e.g., fluid flow rates, to obtain the largest range of saturations with the fewest number of measurements.

Table 1. Properties of the Berea Sandstone Rock Core Used in This Study

Diameter (cm)	Length (cm)	Porosity (%)	Permeability (mD)	Pore Volume (mL)
3.8	20	21	212	47.6

2. Material and Experimental Conditions

A homogenous Berea sandstone rock core was used with the properties summarized in Table 1. The core was 3.8 cm (1.5 inches) in diameter and 20 cm (8 inches) in length. Capillary pressure was characterized on pieces remaining after cutting with the mercury injection capillary pressure (MICP, AutoPore IV 9500, Micromeritics) from vacuum to 227.5 MPa (see Figure 2). The rock core was heated in an oven at 700°C to stabilize mobile clays, standard practice for petrophysical investigations dependent on sequences of observations using the same rock core [*Oak et al.*, 1990]. The mobilized clay can cause time-dependent reduction of rock permeability. The porosity was measured using X-ray imaging, calculated from the difference in X-ray attenuation between a water-filled and air-filled rock. Absolute permeability was measured with a coreflood using distilled water.

To evaluate the impact of pressure, temperature, and brine salinity on residual trapping, corefloods were performed using CO_2 for seven tests and N_2 in one test (both with purity 99%, BOC, Ltd., UK) as the nonwetting fluid and brine with various concentrations of NaCl as the wetting fluid. A range of pressures, temperatures, and brine salinities were explored with the experimental parameters of the tests summarized in Table 2 and Figure 3. Brine salinity ranged from 0 to 5 mol/kg NaCl. The pressure ranged from 5 to 20 MPa. The temperature of the tests was either 25 or 50°C. This resulted in a range of values of interfacial tension from 30 to 47 mN/m for the CO_2 experiments whereas the interfacial tension for the experiment with N_2 was much higher, 73 mN/m.

3. Experimental Design

For this work capillary end effects in corefloods were exploited to rapidly observe the initial-residual saturation relationship across a wide range of saturations at reservoir conditions. Core flooding is an experimental approach whereby multiphase flow properties of a rock, such as the relative permeability, are characterized by observing fluid flow through a sample that is shaped such that the flow can be assumed to be one-dimensional, the so-called rock core. In these tests the inlet and outlet boundaries of core can have an important impact on the design of the test. In these tests the inlet and outlet boundaries of the core can have an important impact on the design of the test. In these locations fluid is moving from or into a region of weak or no capillarity (generally a tube connected to a pump) into or from the rock where capillarity dominates the fluid distribution and provides resistance to flow. In its most common manifestation, the capillary end effect leads to a capillary pressure gradient decreasing toward the outlet of the core resulting in a corresponding saturation gradient from high nonwetting phase saturation at the inlet to low saturation at
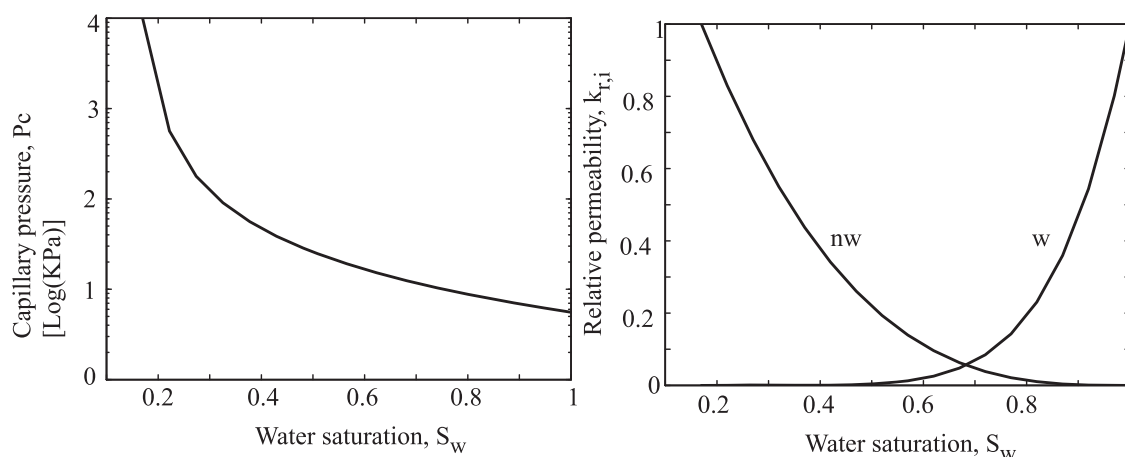

Figure 2. The characteristic capillary pressure and relative permeability curve used to represent Berea sandstone in the experimental design.

Table 2. Experimental Conditions and Fluid Properties for the Eight Experiments Reported in This Work[a]

Exp. Num.	Temp.(°C)	Pressure (MPa)	Molality (mol/kg)	Salinity (mg/L)	IFT (mN/m)	Density[b] (kg/m^3)	Fluid
1	50	10	0	0	36	386	Sc
2	50	10	1	60	37	386	Sc
3	50	10	3	188	41	386	Sc
4	25	10	0	0	34	818	Liquid
5	50	5	0	0	47	105	Gas
6	50	20	0	0	30	784	Sc
7	50	10	5	329	44	386	Sc
8 (N$_2$)	25	10	0	0	73	113	Sc

[a]The text Sc indicates supercritical conditions.
[b]Density is given for the nonwetting phase, either CO_2 or nitrogen.

the outlet. In measurements of relative permeability these effects can cause problems with the interpretation of the results and can lead, for example, to an underestimate of relative permeability at a given nonwetting phase saturation. In characterizing the residual trapping characteristics for this work, however, this effect was used to the advantage of the experiment.

A schematic of the principles of the test is shown in Figure 4. In a given test, a range of initial CO_2 saturations along the length of the core were created by performing drainage at a flow rate that maximized the capillary end effect. Subsequently, imbibition was performed a flow rate representative of reservoir conditions until the saturation reduced to the residual. A range of residual saturations is observed along the length of the core corresponding to the range in initial saturation existing prior to imbibition. As a result, a single coreflood can be used to parameterize the *IR* curve along a range of saturations rather than obtaining a single point along the curve.

For the choice of the specific experimental operating parameters, numerical simulation was used to estimate flow rates that maximized the capillary end effect. Additionally, the simulations were used to identify the combination of flow rates that would allow for a parameterization of the *IR* curve over the largest saturation range in the core with the smallest number of measurements. The numerical model and the resulting optimized test parameters are discussed in the following sections.
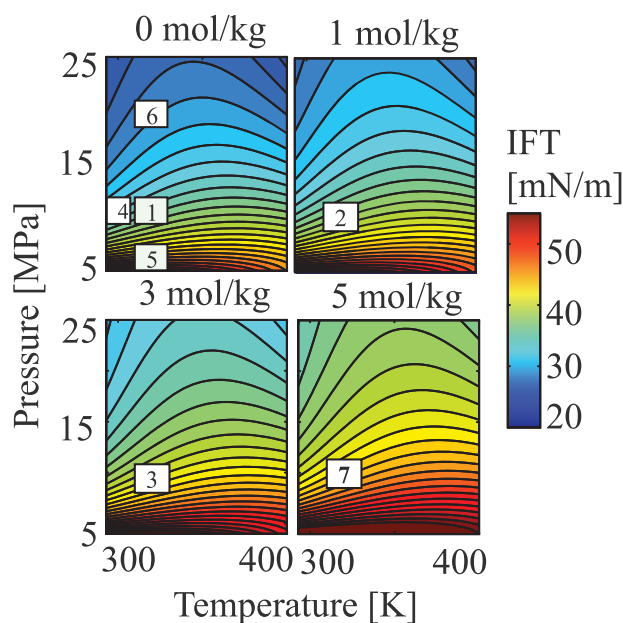
3.1. Description of the Numerical Model

The simulation tool used in this work was the adaptive implicit-explicit black oil simulator (IMEX) from the computer modeling group (CMG). The fluids CO_2 and brine were immiscible by default in the black oil simulator, which was consistent with the conditions created in the trapping experiments in this work. The simulations were performed on a 2-D homogeneous model constructed to represent an axial slice from the middle of the Berea sandstone rock core. The model had 200 grid cells along the flow direction and 50 in the vertical direction. This corresponded to the minimum image thickness obtained from our CT scanner (more details on the experimental setup are available in section 4) and allowed us to assess the potential impact of gravity segregation in the tests. The parameters chosen for physical
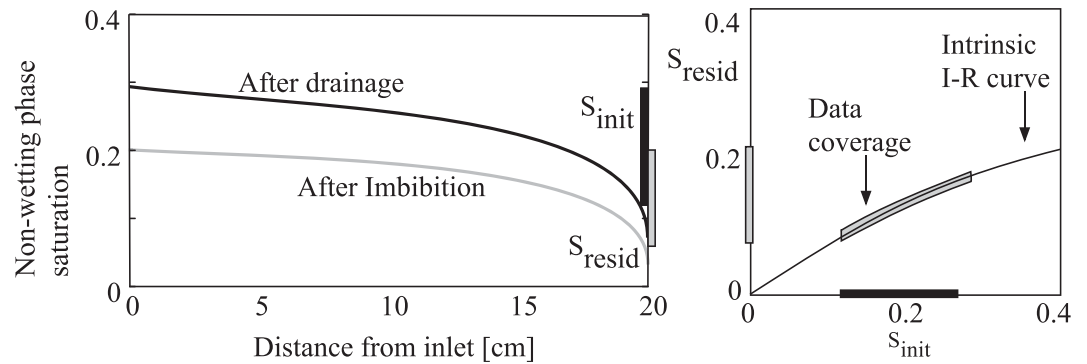

Figure 3. Experimental conditions plotted on a map of IFT as a function of pressure and temperature at the brine salinities (NaCl) used in this study.

Figure 4. Schematic showing the technique for the rapid construction of the residual trapping curve. A drainage coreflood is performed and X-ray imaging used to obtain saturation along the core (left). Using drainage flow rates that optimize the capillary end effect, a range of initial CO_2 saturations can be imaged in the core prior to imbibition. Upon imbibition the saturation lowers and the *IR* curve is constructed (right) correlating the final saturation in each slice along the core to the saturation prior to imbibition.

properties in the model are described in Table 3. The experimental conditions of experiment two were used as input for the simulation.

The Brooks-Corey model was used to describe the relative permeability and is shown in equations (4) and (5), where the $S_{w,irr}$ is the irreducible water saturation and the parameters n_w and n_{CO_2} are Corey exponents for brine and CO_2, respectively. The characteristic relative permeability used in the model was chosen to represent data from experiments on relative permeability in Berea sandstone reported in *Krevor et al.* [2012] and *Kuo et al.* [2010] and shown in Figure 2.

$$k_{r,w} = \left(\frac{S_w - S_{w,irr}}{1 - S_{w,irr}}\right)^{n_w},$$ (4)

$$k_{r,CO_2} = \left(\frac{1 - S_w - S_{CO_2,r}}{1 - S_{w,irr}}\right)^{n_{CO_2}}.$$ (5)

The capillary pressure values for the mercury air system, $P_{c,Hg}$, collected using MICP were used to estimate the capillarity of the CO_2-brine, P_{c,CO_2}, system using the conventional Young-Laplace scaling (equation (6))

$$\frac{P_{c,CO_2}}{P_{c,Hg}} = \frac{\sigma_{CO_2 - H_2O}}{\sigma_{Hg - air}},$$ (6)

where it was assumed that the wetting properties of the two systems were similar. After conversion, the data were fit with the Brooks-Corey model [*Li*, 2004] for use in the simulator,

$$P_c = P_e (S_*)^{-1/\lambda},$$ (7)

where P_e was the entry pressure for the invasion of CO_2 into the core sample, and λ the pore size distribution index. The fitted value of P_e and λ used in the simulation were 5.5 kPa and 0.6, respectively. Figure 2 shows the capillary pressure curve used in our simulation.

Boundary slices were added to both inlet and outlet ends of the core, having the same dimension and properties as the rock slices following a procedure outlined in *Kuo et al.* [2010]. Constant injection rate-controlled wells and constant bottomhole pressure controlled wells were completed in the grid elements of

Table 3. Parameters Used in the Experimental Design Simulation

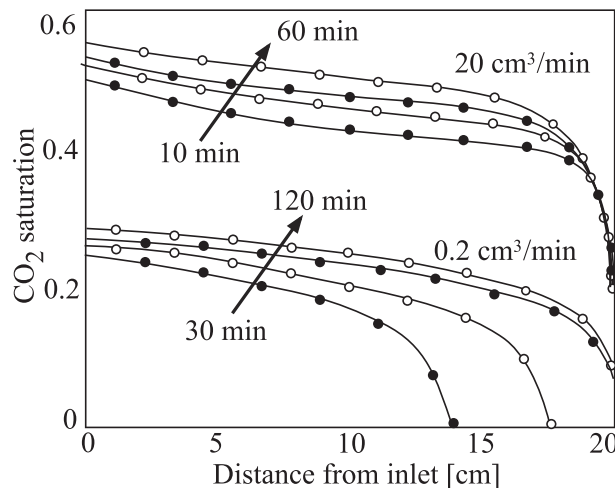| Properties	Units	Values	Properties	Units	Values	Properties	Units	Values
Porosity	(%)	18.8	Core length	(cm)	20	S_{wr}		0.1699
Permeability	(mD)	212	Temp.	(°C)	50	S_{nwr}		0
Core diameter	(cm)	3.8	Pressure	(MPa)	10	λ		0.6
ρ_w	(kg/m³)	1023.6	Salinity	(mol/kg)	1	n_w		6
ρ_{co_2}	(kg/m³)	385.5	μ_{co_2}	(cP)	0.028	n_g		3
σ	(mN/m)	37.37	μ_w	(cP)	0.609	P_e	(KPa)	5.5

Figure 5. Simulated saturation profiles along the core sample during drainage with injection rates 0.2 and 20 cm^3/min and various amounts of time.

the inlet and outlet boundary slices, respectively. In addition, linear relative permeabilities were used for the inlet and outlet slices to allow full mobility for each phase. The capillary pressure between CO_2 and brine was set to zero at the inlet. For the outlet boundary the capillary pressure was set to a constant equal to the entry capillary pressure P_e. While there is still some debate as to how best to represent the capillary discontinuity in a physical sense [*Richardson et al*., 1952], this arrangement produced simulation results most consistent with our observations of the impact of the inlet and outlet boundaries.

3.2. Optimum Fluid Velocities

Simulation results for CO_2 saturation along the length of the core after injection into an initially brine saturated core are shown in Figure 5 for injection rates 20 and 0.2 cm^3/min. Each point represents the CO_2 saturation averaged across the entire slice. As anticipated, the CO_2 saturation decreased toward the outlet due to the capillary end effect, resulting in a range of initial saturations prior to imbibition. In Figure 6, a histogram of saturation values achieved after 60 min of drainage are shown for four flow rates. In this scenario four cycles of drainage, imbibition and core refreshing would result in an initial-residual characteristic trapping curve spanning initial CO_2 saturations from 0.15 to 0.65 with most of the data coverage at intermediate values. Optimal flow rates were seen as those that maximized the saturation range of observations with the smallest number of experimental cycles. For the experimental observations two drainage injection rates were thus chosen, 0.2 cm^3/min to obtain initial saturations at a lower range of values and 20 cm^3/min to obtain initial saturations at a higher range of values. In the simulation this resulted in a small gap in initial
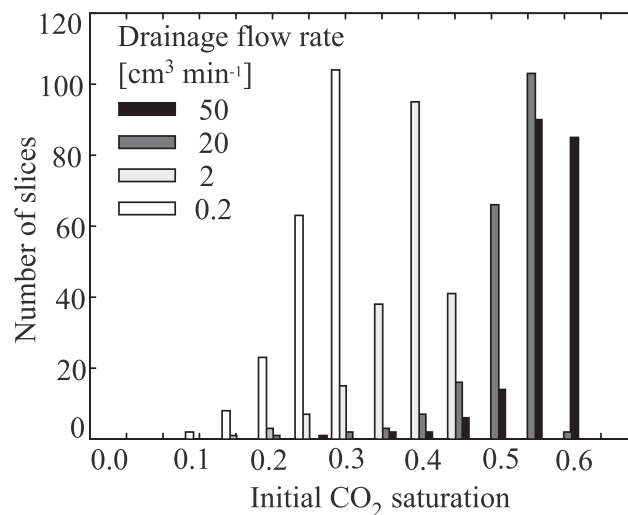

saturation values from 0.3 to 0.4, in Figure 6. This was sometimes observed in the experiments although in some measurements continuity in the observations obtained at the low and high flow rates was observed. Figure 7 shows the simulated data on the *IR* curve. The initial values are taken from the simulated CO_2 saturation profile and the residual values are related to the initial saturation through the *Land* trapping model with coefficient $C = 1.1$ after previous CO_2 observations of residual trapping by *Krevor et al.* [2012]. A drainage injection rate of 0.5 cm^3/min was used for some experiments to provide data coverage to show continuity between data gathered using low and high drainage rates. Similarly, some brine injection rates of 0.5 cm^3/min for imbibition were

Figure 6. A frequency histogram of the simulated average CO_2 saturation after 60 min of drainage. Each data point is the average saturation over the entire diameter of the core and 1 mm in the axial direction, referred to as a "slice" in the plot. The plot shows how a range of saturations can be covered utilizing different drainage flow rates. It also shows that there will be more data coverage for the intermediate saturation values. In the experiments saturations with less than 10 slices worth of data were ignored.
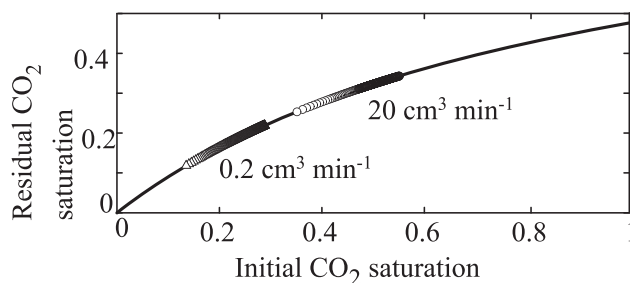
Figure 7. Simulated data on an initial-residual curve plot for two drainage flow rates.

chosen to test the impact of different imbibition rates on the results. Full details of the experiments are included in section 4. It was found that within this range of variation there was no impact of injection rate on the results of the tests.

In choosing flow velocities it was of primary concern that drainage and imbibition processes occurred in a force balance regime where capillarity dominates the pore-scale distribution of the fluids. For Berea sandstone this has been observed in several studies to be in the range where N_c $< 10^{-5}-10^{-4}$ [*Taber*, 1969; *Foster*, 1973; *Gupta and Trushenski*, 1979]. The capillary numbers associated with the experimental test parameters are listed in Table 4 with the viscosity associated with the displacing phase, CO_2 during drainage and brine during imbibition. All of the experiments were well within the capillary dominated regime. The capillary numbers were also similar to values observed in field settings during water flooding, where N_c varies between 10^{-7} and 10^{-6} [*Lake*, 1989].

4. Experimental Setup and Procedures

4.1. Experimental Setup

The experimental work was conducted on a coreflooding system recently developed at Imperial College London. The system used in this work included, six pumps, a two phase separator, differential pressure transducers, and a core holder, as shown in Figure 8. All wetted parts were made of HC276 hastelloy. The experimental setup was a closed loop system which allowed for a preequilibration of mass transfer between CO_2 and brine prior to the initiation of drainage in the rock core. The system allowed fluids to be coinjected into the core sample at maximum pressure of 30 MPa and temperature 120°C.

Each of the pumps (Teledyne Isco, model 500D) used for the injection of fluids and to maintain the overall pressure in the system had a volume capacity of 507 mL and flow range from 0.001 to 204 mL/min. The temperature of the fluid in the pumps was controlled by external fluid circulation temperature control baths connected to the pumps. All of the tubing in the rig was heated by resistance heating lines and wrapped in insulating foam. The effluent of the core was sent to a two-phase separator (Vinci Technologies) with a 500 mL capacity, housed in an oven. The fluid interface in the separator was monitored thorough a sapphire window by an automated moving camera with software programed to locate the interface and move the camera synchronously as needed to keep track of the interface. The system pressure was controlled by a pump in constant pressure mode and separate pairs of pumps were used to circulate CO_2 and brine in a dual pump operation where the two pumps for a given fluid were simultaneously injecting fluid into the rock core while retrieving fluid from the two-phase separator. To confirm the correct operation of the circulating system data from all pumps and the two-phase separator were recorded in real time and displayed on a central computer in a control room where it could be monitored while X-ray imaging was taking place. The core holder used was a Phoenix Instruments aluminum core holder wrapped in a silicone heating tape with temperature measured in the confining fluid to maintain the core at the desired temperature. A confining stress was applied with water as the confining fluid using a pump (Teledyne Isco, Model 100DX) that had a pressure limit of 69 MPa. Two high-accuracy pressure transducers (Oil filled Digiquartz Intelligent transmitter, Model 410K-HT-101) were connected through tubing ported directly to the inlet and outlet faces of the core to measure the pressure drop across the core. A Universal Systems HD-350 X-ray CT scanner was used for in situ saturation

Table 4. Capillary Number N_c Ranges for the Flow Rates Used in the Experiments

Injection Process	Rates (cm³/min)	N_c [a]
Drainage	20	$(5.3-34) \times 10^{-7}$
Drainage	0.5	$(1.3-8.5) \times 10^{-8}$
Drainage	0.2	$(5.3-34) \times 10^{-9}$
Imbibition	0.2	$(1.7-3.9) \times 10^{-7}$
Imbibition	0.5	$(4.3-9.7) \times 10^{-7}$

[a]The variation is due to changes in thermophysical properties of the fluids among test conditions.
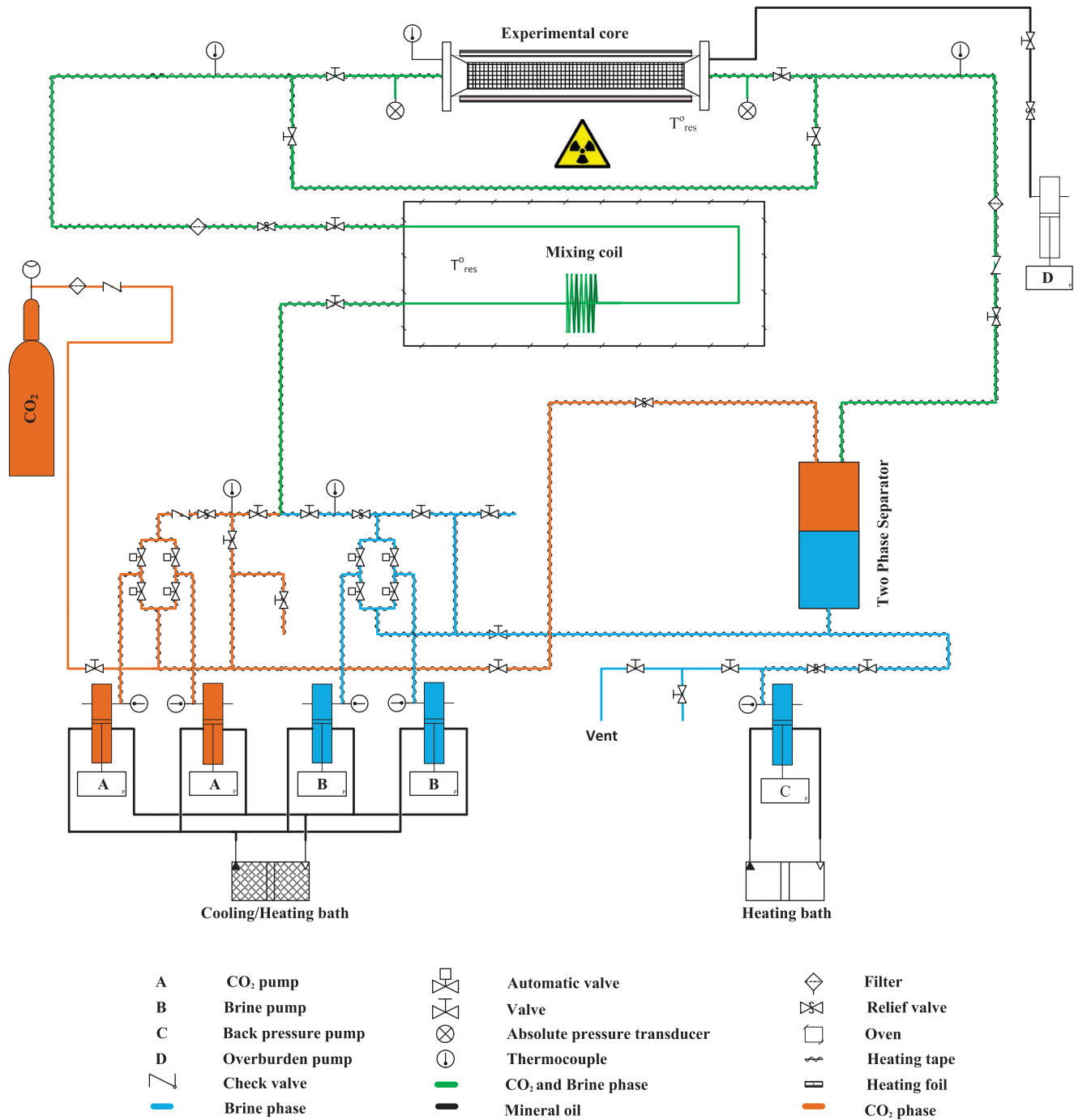
Figure 8. Schematic of the experimental setup used in this work.

monitoring during the tests. The size of the scanned images was 512 × 512 pixels, with the dimensions of each pixel 250 μm.

4.2. Porosity and Saturation Measurement

Porosity and saturation were calculated using the standard procedure involving a calibration for each test with CT scans of the core fully saturated with the fluids at the pressure, temperature, and brine salinity conditions of the test [*Akin and Kovscek*, 2003]. Equations (8) and (9) show the calculations used based on the calibration observations. In the equations, *CT* refers to the measured X-ray attenuation in Hounsfield units for each pixel. The variables $CT_{w,r}$, $CT_{a,r}$, $CT_{CO2,r}$, and CT_{br} are the CT number of the core fully saturated with
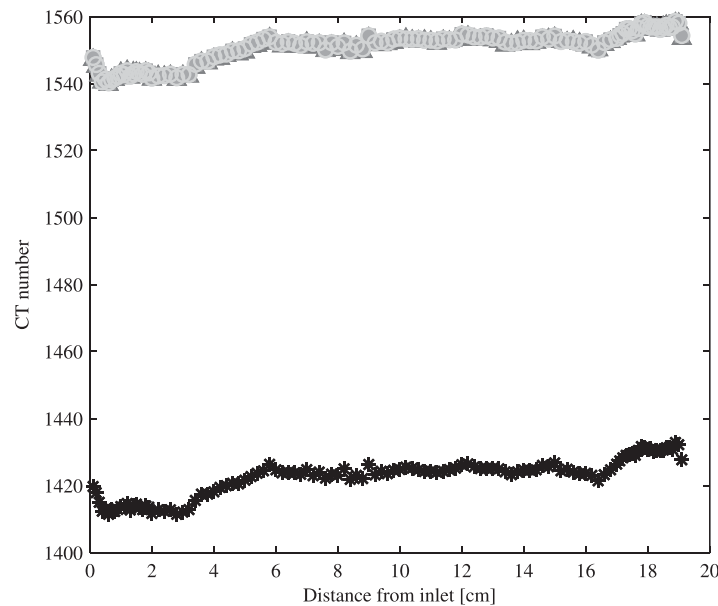
Figure 9. Comparison of CT numbers before and after CO_2 fully dissolved into the brine in Exp. 1. Star: CO_2 saturated core, triangle: after 4.3PVI, square: after 5.6PVI, circle: after 6.9PVI.

deionized water, air, CO_2 and the CO_2-saturated experimental brine, respectively. The CT number of the two pure reference fluids is CT_w and CT_a for water and air, respectively. The variable CT_{ex} is the CT number of an image of a partially saturated core during an experiment

$$\phi = \frac{CT_{w,r} - CT_{a,r}}{CT_w - CT_a}, \qquad (8)$$

$$S_{CO_2} = \frac{CT_{ex} - CT_{br}}{CT_{CO_2,r} - CT_{br}}. \qquad (9)$$

The values for the two pure reference fluids, CT_w and CT_a, were close to 0 and -1000 for each scan. In our calculation equations (8) and (9) were applied to calculate slice average properties by using slice-averaged CT numbers. The voltage and current used in the experiment were 120 kV and 225 mA, respectively. The X-ray exposure was 1 s for each slice.

4.3. Experimental Procedures

The experimental setup was a closed loop and prior to inserting the core holder, the system was purged of ambient air using degassed water. Subsequently, CO_2 circulation was used to clear water from lines that would be used for CO_2 circulation to avoid premature introduction of water into the rock core.

For each test the fired Berea sandstone rock core was dried in a vacuum oven at 60°C for at least 12 h. The dry core was then wrapped with an inner layer of heat shrinkable 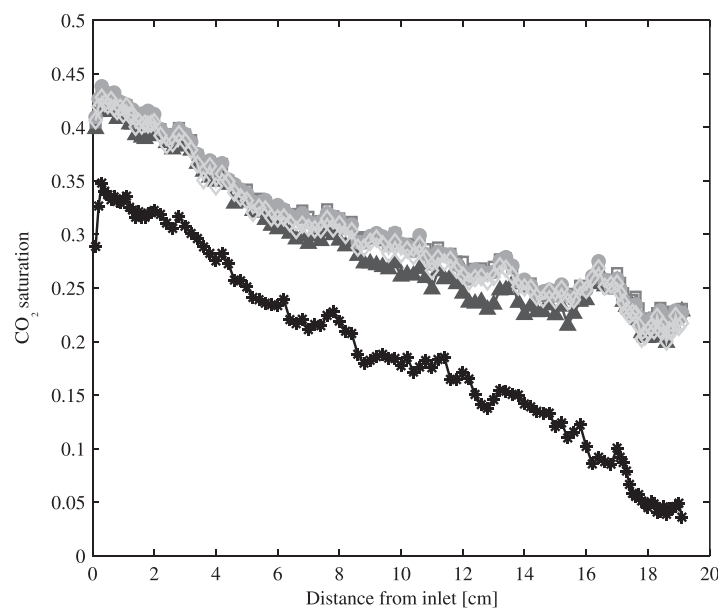teflon, a central layer of aluminum foil, an outer layer of teflon and finally housed in a viton sleeve. The teflon prevented bypassing channels along the sleeve of the core while the aluminum prevented diffusion of the CO_2 into the Viton and confining fluid. This assembly was then inserted into the core holder. The core was flushed with dry gaseous CO_2 and an overburden pressure of 5 MPa was applied through the confining fluid. At this stage, the core was scanned to obtain $CT_{a,r}$. The thickness of the imaged slice was 1 mm in all of the experiments.

Figure 10. The CO_2 saturation along the core during the drainage process in Exp. 1, at 0.2 cm³/min. Star: 0.16PVI, triangle: 0.29PVI, square: 0.42PVI, circle: 0.55PVI, diamond: 0.68PVI. All PVI data calculated from the moment CO_2 entered the core.

Based on our simulation results (Figure 5) the saturation varied more rapidly close to the inlet and outlet ends of the core and slowly in the central
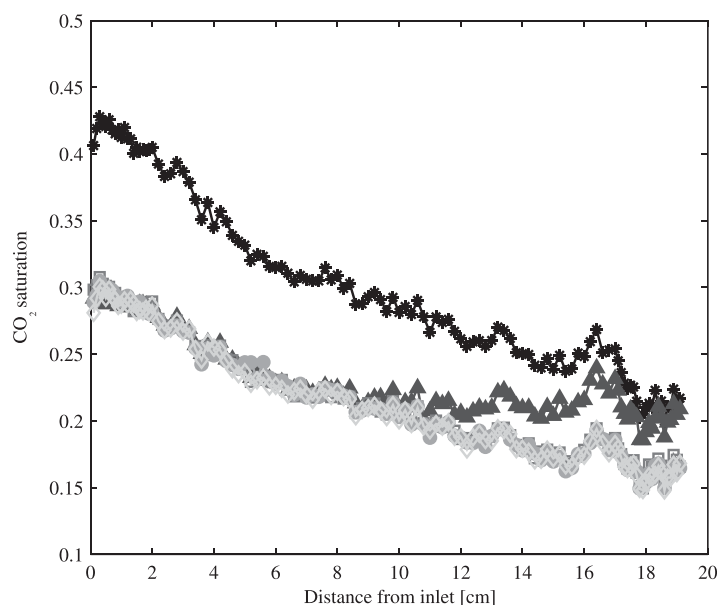
Figure 11. The CO_2 saturation along the core during the imbibition process in Exp. 1, at 0.2 cm^3/min. Star: initial CO_2 saturation, triangle: 0.09PVI, square: 0.22PVI, circle: 0.35PVI, diamond: 0.57PVI (residual CO_2 saturation).

region. Therefore, scans were taken averaging over 1 mm thickness for the 20 mm closest to the inlet and outlet ends while scans in the central section were taken with spacing of 2 mm between slices. This allowed for observations across the entire core to be obtained within 15 min without having to stop to wait for the X-ray tube to cool.

The core sample was first saturated with dry CO_2. The system was then pressurized and heated to the experimental conditions. When the CO_2 was equilibrated in the core holder with the pressure and temperature the core was scanned to obtain $CT_{CO_2,r}$. The core was then saturated with brine injected into the core at 2 cm^3/min. Most of the CO_2 flowed out of the downstream end of the core and the remaining CO_2 dissolved into the brine. Figure 9 shows the CT values obtained in experiment 1 while verifying that CO_2 had either left the core or fully dissolved into the brine after approximately five pore volumes of brine injected.

At this point, the core holder was isolated by closing off valves and circulating fluid through a line bypassing the core holder (Figure 8). The CO_2 and brine were then equilibrated by cocirculating the fluids together for 10–12 h while the volume balance of fluid in the system was monitored. The total volume of fluid in the system reached a steady state after a few hours providing a confirmation that no further net dissolution was occurring.

Before starting CO_2 injection, the brine in the core was replaced with CO_2 saturated brine and the core was scanned to obtain CT_{br}. To perform the drainage step, CO_2 was injected into the equilibrated brine saturated core at the low drainage rate, 0.2 or 0.5 cm^3/min, for the test. Due to the dead volume of tubing between the CO_2 pump and core holder it typically took around 1 h for CO_2 to reach the inlet of the core sample. The simulation results indicated that breakthrough should take place after approximately 40 min of drainage (Figure 5), and at that time the whole core was scanned. The scanning itself occurred over a duration of 15 min and a subsequent 15 min was required for the X-ray tube to cool before scanning could begin again.

From this point, the whole core scanning was continuous until the end of the imbibition cycle. During drainage, a minimum of two sets of the whole core scans were taken which provided a confirmation that the saturation was not changing during the duration of the scans and that the initial CO_2 saturation prior to imbibition was accurately captured, shown in Figure 10. The imbibition process was initiated by injecting brine. The actual CO_2 drainage injection process continued until the brine reached the core sample, typically requiring 1 h further, during which time scans continued to insure that the correct initial CO_2 saturation was obtained. The measurement of residual CO_2 saturation was made after the saturation profile was confirmed as stable, shown in Figure 11. As anticipated from the simulation design, the capillary end effect allowed for a large saturation range to be observed at the low drainage flow velocities.

Before starting drainage for the high injection rate (20 cm^3/min) phase of the test, the core was flushed with distilled water and resaturated with the equilibrated brine, to make sure all experiments represented a process of primary drainage and secondary imbibition. The experimental setup allowed for the replacement
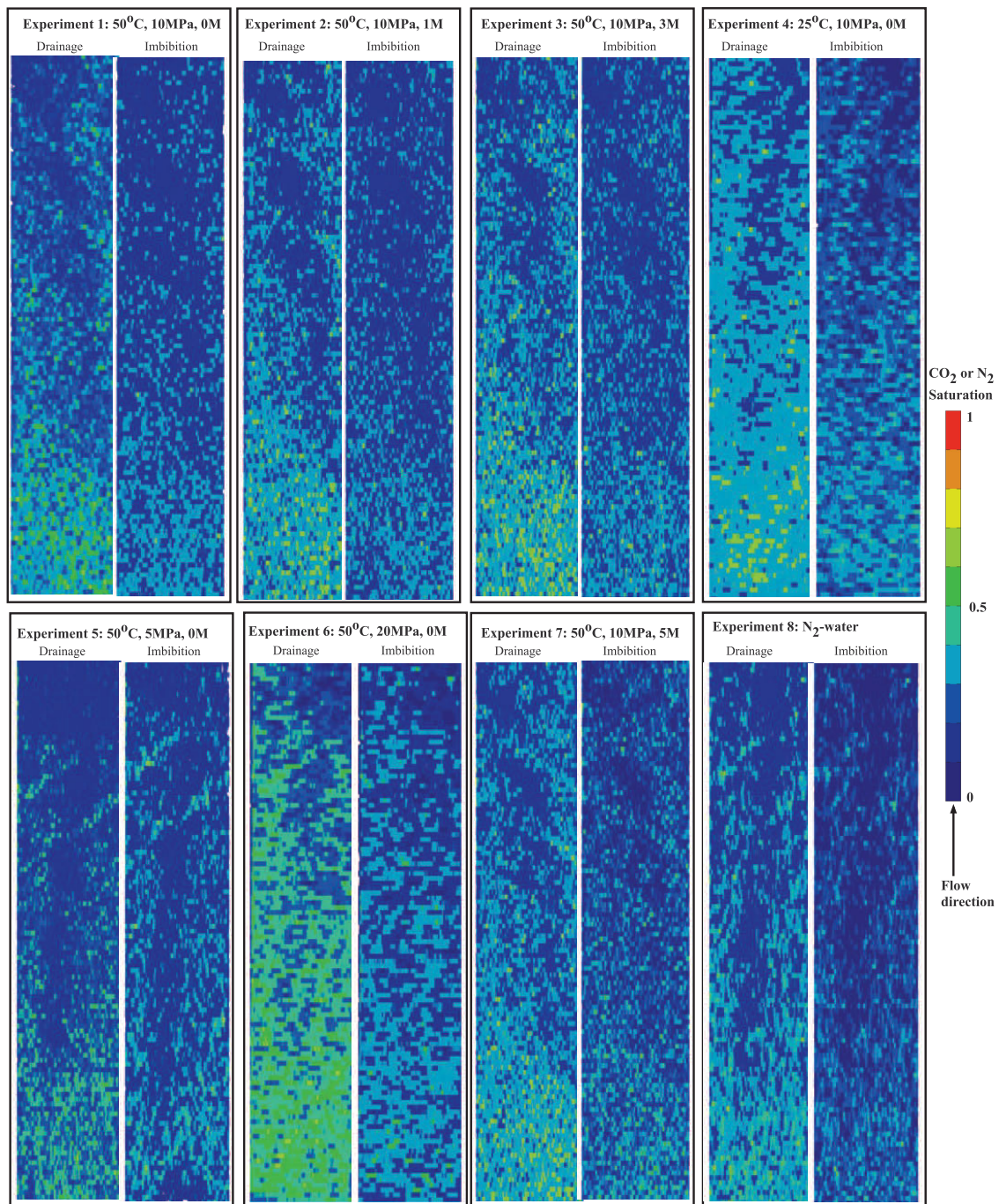
Figure 12. Saturation maps for all conditions after drainage at 0.2 or 0.5 cm^3/min and imbibition at 0.2 or 0.5 cm^3/min (the size of the reconstructed images was 115 × 116, with the dimensions of each pixel 250 × 2000 μm).

of part or all of the brine in the system while maintaining pressure and temperature conditions throughout the system. The procedures for the high injection rate drainage process followed those for the low injection rate drainage.

The use of heating lines and insulation to maintain temperature in the tubing at the size scale of a coreflooding rig is known to have limitations in precision and control [*Braun*, 2011]. Thus the general approach taken for temperature controlled corefloods was to rely on heating lines and insulation to maintain the temperature within a ±10°C range but to obtain precision in the temperature, ±0.5°C,
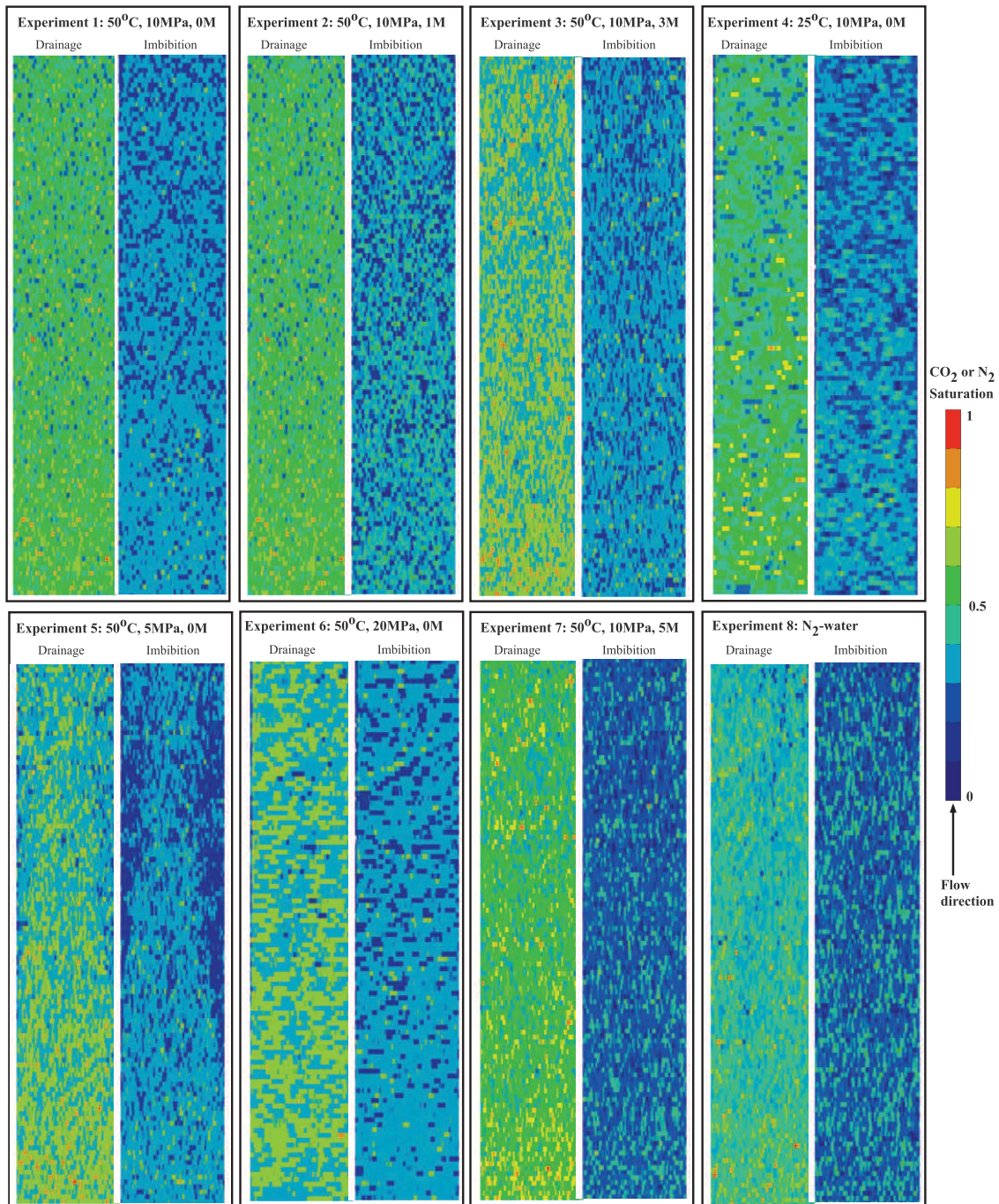
Figure 13. Saturation maps for all conditions after imbibition at 20 cm^3/min and imbibition at 0.2 or 0.5 cm^3/min (the size of the reconstructed images was 115 × 116, with the dimensions of each pixel 250 μm× 2000 μm).

with heating baths and ovens in the lines just prior to the inlet of the core, in the core itself and in other locations (pumps and separator) where large fractions of the fluid are concentrated in a single location. In practice, small amounts of mass transfer between CO_2 and brine during imbibition is often observed in these experiments as well as all others that report in situ saturation monitoring [*Lu et al.*, 2011; *Akbarabadi and Piri*, 2013]. We made a number of observations to quantify the issue for our system and a detailed summary of the findings are provided in the Appendix A. In all cases the dissolution of CO_2 occurred as a slowly moving front beginning at the upstream end of the core (see Figure A1 in
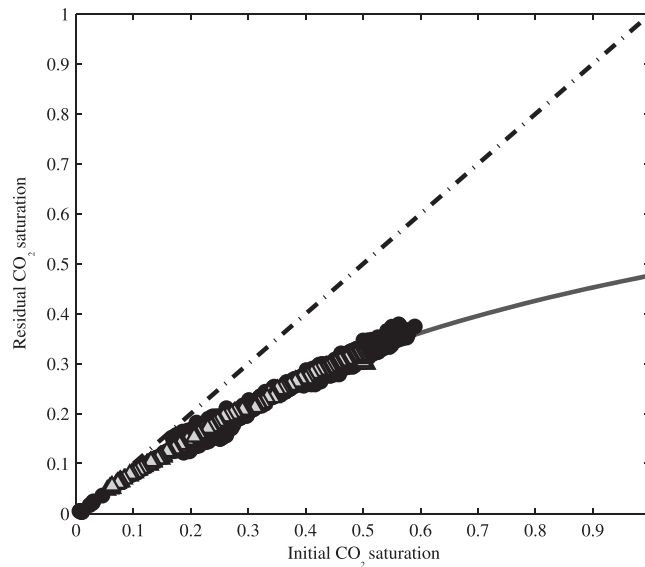
Figure 14. Data from all of the experiments on a single *IR* plot with a model curve from the *Land* model with constant *C* = 1.1. The triangles are the N_2-water data set and the black circles are the compiled data from the CO_2 tests. The dashed line shows the 1:1 line.

the Appendix A) and scaled linearly with the number of pore volumes of brine injected. This was indicative of a system in which the incoming brine was slightly undersaturated with respect to the CO_2 in the core. The level of undersaturation was small and constant during imbibition such that hundreds of pore volumes were required to dissolve all of the CO_2. The important feature of the dissolution process with respect to characterizing residual trapping was that while trapped CO_2 was slowly removed from the upstream part of the core, the downstream saturation remained constant over the course of hundreds of pore volumes until reached by the dissolution front, confirming that this characterized the saturation of a stable residually

trapped phase. Additionally, the areas in the core where CO_2 has dissolved into brine are readily visible from the 3-D CT scan images (see Figure A2 in the Appendix A). Thus, all data characterizing the IR characteristic curves were easily taken from downstream sections of the core that were identifiably unaffected by dissolution at the time of scanning.

5. Results and Discussion

Figures 10 and 11 show the evolution of the CO_2 saturation during drainage and subsequent imbibition. In all cases a residual CO_2 saturation was obtained quickly, with less than one pore volume of brine injected,
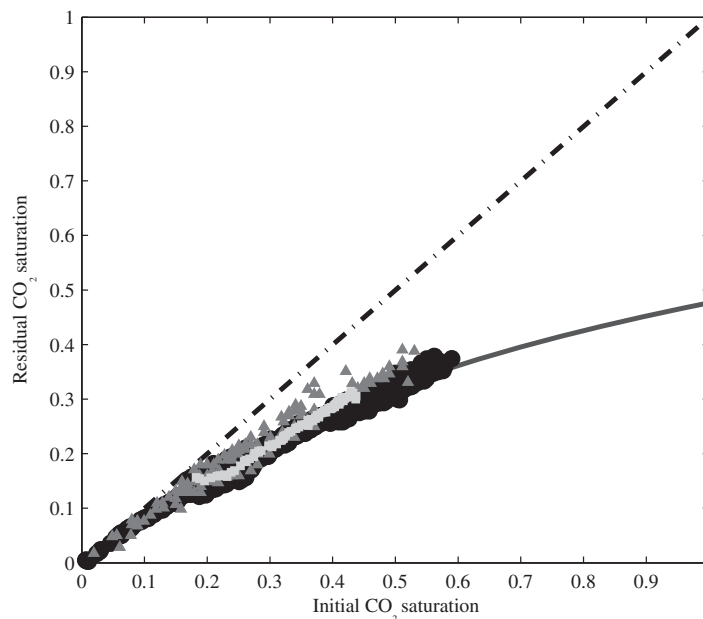

Figure 15. The compiled plot of the data from this work compared with data reported in the literature. Triangle: data from *Akbarabadi and Piri* [2013], square: data from *Krevor et al.* [2012], black line: *Land*'s model with *C* = 1.1.

remaining stable for up to 40 pore volumes of brine injected. This rapid desaturation process is characteristic of a water wet system and is often used as an indicator that the system is water wet [e.g., *Salathiel*, 1973].

Saturation maps from the central slice of the core are shown for all of the experiments after drainage and imbibition in Figures 12 and 13 for the low and high drainage flow rates, respectively. Random noise in the X-ray imagery results in a quantifiable uncertainty in the saturation value for a given pixel. For comparison purposes some of the images were coarsened (averaging over several pixels) following a procedure outlined in *Pini et al.* [2012] so the uncertainty in the saturation
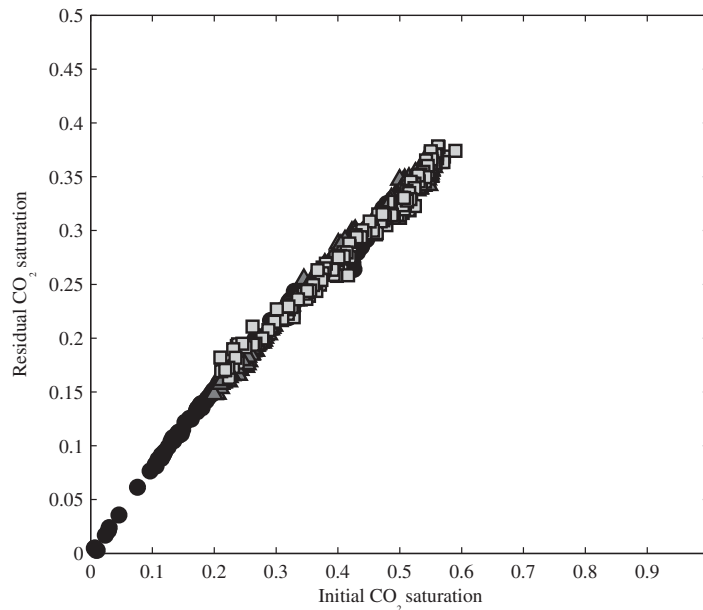
Figure 16. The *IR* plots for experiments with distilled water at 50°C and various pressures: circle: Exp. 5, 5 MPa, upward-pointing triangle: Exp. 1, 10 MPa, square: Exp. 6, 20 MPa.

value of a pixel in all of the images are in the range 0.11–0.13. This was particularly the case for experiments 4 and 6, where the density difference between CO_2 and brine were quite low. More details on the uncertainty characterization are provided in an Appendix B. Images from experiments at the same temperature and pressure are most directly comparable. In particular, a comparison of the saturation maps after drainage at the low flow rates during experiments 1, 2, 3, and 5 show that the spatial distribution of the saturation within the core were nearly identical between experiments, showing the high degree of repeatability that was obtained in the corefloods. The distribution in experiment 5

after imbibition shows some heterogeneity. This experiment was with gaseous CO_2 and the condition most susceptible to small-scale heterogeneity in the core. Generally, the saturation maps and particularly those at high drainage flow rates show the uniformity of the rock core with the CO_2 evenly distributed throughout the core in all of the experiments.

A compilation of the *IR* data from all of the floods in Figure 14 shows that there was little if any impact of reservoir conditions on the residual trapping characteristics of this system. The N_2-water curve was also indistinguishable from the CO_2-brine curves, suggesting that this was an intrinsic property of the rock, insensitive to fluid pairs and reservoir conditions in which the system is strongly water wet and the distribu-
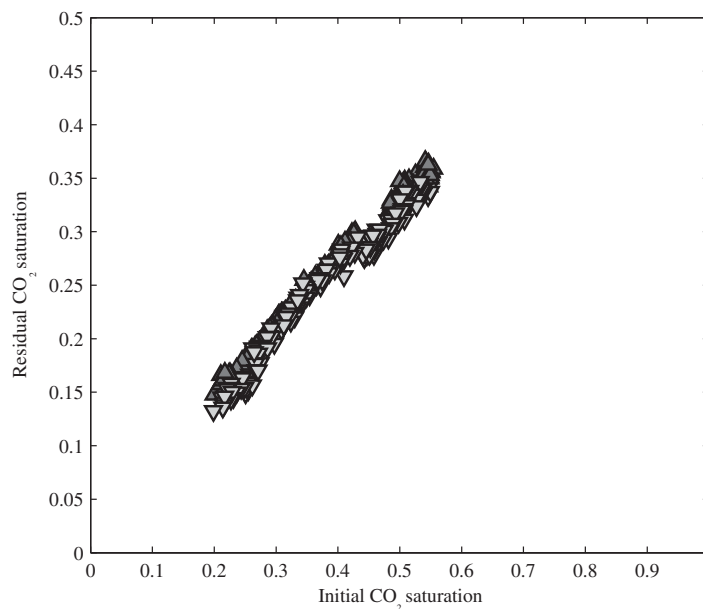
tion of fluid is dominated by capillary forces. A comparison between the compiled data set from this work and *IR* curves measured on Berea sandstone in different laboratories reported in *Akbarabadi and Piri* [2013] and *Krevor et al.* [2012] is shown in Figure 15. The data are remarkably similar and demonstrate the strength of the *IR* curve as a characteristic property of multiphase flow for a rock type. Subsets of these compiled results are discussed, focusing on pressure, temperature, and salinity variation in the following sections.

Experiments, 1, 5, and 6 were carried out at pressures of 10, 5, and 20 MPa pore pressure,
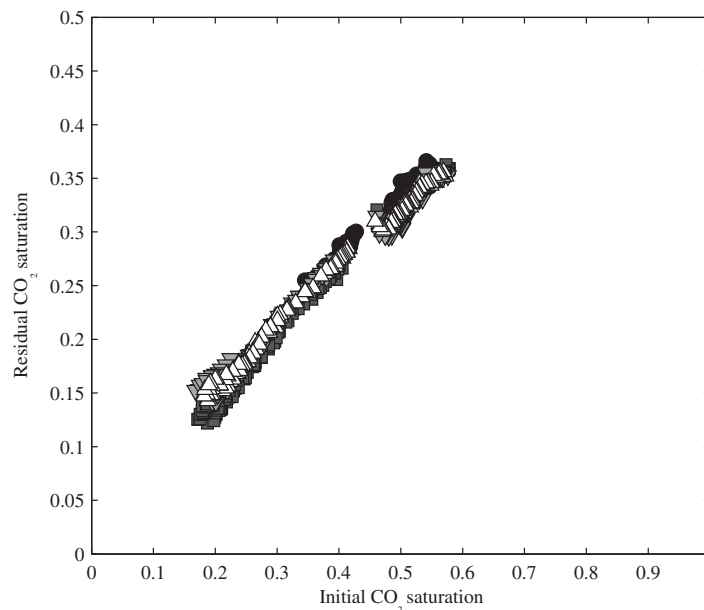

Figure 17. The *IR* plots for experiments at 10 MPa and two temperatures: upward-pointing triangle: Exp. 1, 50°C, downward-pointing triangle: Exp. 4, 25°C.

Figure 18. The *IR* plots for experiments at 10 MPa, 50°C and different salinities: circle: Exp. 1, 0M, square: Exp. 2, 1M, down-pointing triangle: Exp. 3, 3M, up-pointing triangle: Exp. 7, 5M.

respectively (Table 2 and Figure 3), and Figure 16 shows the *IR* characteristics without any discernible impact of the variation in conditions. Similarly the results of experiments 1 and 4 were performed at 50 and 25°C, respectively, and the results in Figure 17 suggest that temperature had little impact as the CO_2 phase transitioned from a supercritical to a liquid fluid.

The contact angle for CO_2-brine-silica system has been observed to vary with salinity [*Chiquet et al.*, 2007; *Espinoza and Santamarina*, 2010; *Broseta et al.*, 2012; *Jung and Wan*, 2012]. Figure 18 shows the *IR* data plot for experiments 1, 2, 3, and 7 in which the salinity was varied from no salt content to 5M NaCl. Again, the results suggest that any effect is not strong enough to play an important role in controlling the multiphase flow properties.

In the case of the N_2 coreflood with distilled water at 25°C and 10 MPa pore pressure, the viscosity and density of N_2 were similar to CO_2 at 50°C and 50 MPa (Table 2). The solubility of N_2, 1.3 cm^3/g [*Wiebe et al.*, 1933], however, is nearly 25 times lower than CO_2, 32 cm^3/g (cm^3 of gas at standard conditions per gram of water) [*Wiebe*, 1941]. Therefore, the nitrogen is equilibrated with water more quickly and easily from an experimental standpoint than with the CO_2. Add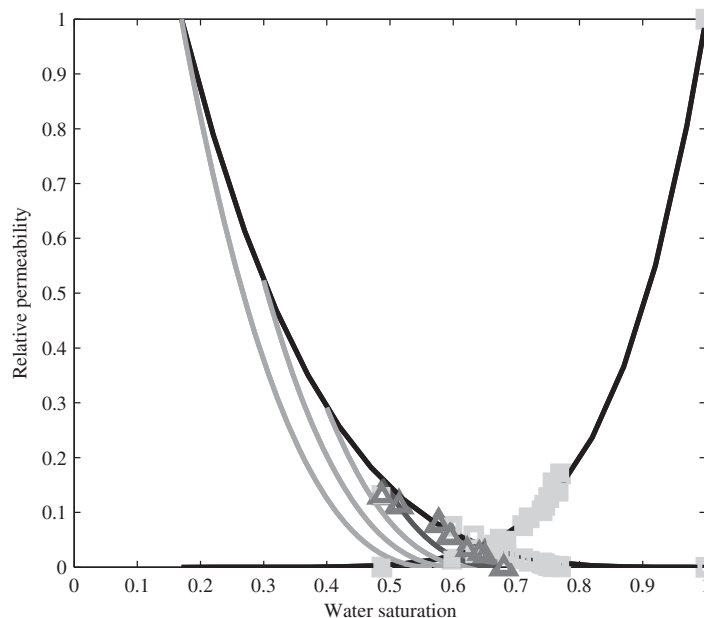itionally, avoiding the use of corrosive fluids significantly decreases the demands on the experimental apparatus. It is possible thus that the residual trapping efficiency for CO_2-brine in sandstone could be estimated using a N_2-water system where the experimental apparatus for handling CO_2-brine systems is not readily available. Indeed, it is likely that other fluid pairs useful in creating other analog values of viscosity and density could also be used so long as they were strongly water wet in sandstone.

Figure 19. Drainage relative permeability and imbibition scanning curves for Berea sandstone. The squares represent water (closed) and CO_2 (open) drainage relative permeability measurements. The two open triangles highlight an initial-residual saturation pair. Black lines: drainage curve fit using the Brooks-Corey model. Gray lines: imbibition curves generated using the *Land* equations.

To illustrate the use of the *IR* data for parameterizing hysteresis, a drainage steady state relative permeability characterization was performed on the same rock core at 10 MPa and 50°C with the same experiential setup. More details on the

Table 5. Properties of the Fired Berea Sandstone Used in the Test Experiment

Diameter (cm)	Length (cm)	Porosity (%)	Permeability (mD)	Pore Volume (mL)
3.8	19	16.5	73	35.9

experimental procedures for steady state relative permeability experiments can be found in *Krevor et al.* [2012] and B. Niu et al. (The impact of fluid properties and flow conditions on the measurement of relative permeability for CO_2-brine system, unpublished manuscript, 2014). Figure 19 shows the experimental data and best fit curves based on the Brooks-Corey model (equations (4) and (5)). The best fit parameters n_w and n_g were 5.9 and 3.8, respectively. In the data fitting, the endpoint drainage relative permeability was assumed to be one for lack of precise observations at the endpoint. Figure 19 shows the bounding imbibition scanning curves for CO_2 generated by the *Land* model with the value $C = 1.1$ corresponding to the experimental data obtained in this work.

It is important to note that the scope of this work was to evaluate the impact of reservoir conditions on capillary trapping in homogenous rocks. Indeed, the parameterization of hysteresis using the *IR* curve is applicable to homogeneous domains. A number of recent studies have also made clear the importance of capillary heterogeneity in reservoir rocks leading to CO_2 immobilization that is not well described by a simple parameterization with a single *IR* curve [*Li and Benson*, 2014; *Gershenzon et al.*, 2014; *Krevor et al.*, 2011; *Saadatpoor et al.*, 2010]. In this case, the immobilization can be modeled using numerical simulation populating the petrophysical domains of the heterogeneous system with specific *IR* curves obtained from homogenous samples representative of the individual domains. Alternatively upscaling can be applied to obtain effective or pseudoparameters for domains that include known heterogeneity. Thus far, there is no standard technique for making trapping observations for use in modeling that incorporates the presence of heterogeneities in the rock sample itself.

6. Conclusion

We have used a coreflooding experimental approach to obtain observations of residual trapping in the CO_2-brine-sandstone rock system at a range of conditions and fluid properties representative of reservoirs targeted for CO_2 storage. A novel residual trapping test was developed using in situ saturation monitoring to rapidly observe a wide range of initial CO_2 saturations in a core during a single flood, making use of the capillary end effect. A simulation approach to the design of the experiment proved useful for choosing the optimum injection rates for the drainage process. The observed residual trapping characteristic curve was found to be invariant across a wide range pressures, temperatures, and brine salinity conditions, including a comparison with a flood using a N_2-water system. The results suggested that the system was strongly water wet and also that the use of analog fluids for this characterization may be useful when the full reservoir conditions cannot be replicated in the laboratory. The rapid *IR* characterization may also be useful as a first-order characterization of hysteresis in the multiphase flow properties.

Appendix A: The Impact of Mass Transfer on Residual Trapping Observations

In these experiments mass transfer, with CO_2 dissolving into brine, was observed when the imbibition process was performed for extended periods of time. This has also been reported in other CO_2-brine residual trapping tests that include in situ saturation monitoring [*Lu et al.*, 2011; *Akbarabadi and Piri*, 2013]. We performed a number of tests to evaluate the source of the disequilibrium and to evaluate the potential impact of mass transfer on the results.

The dynamics of the dissolution were observed in three experiments labeled A, B, and C at 14 MPa and 60°C with brine salinities 5, 3, and 0M NaCl, respectively. A less permeable Berea sandstone rock was used to increase the pressure variation across the core and the properties of the rock sample are shown in Table
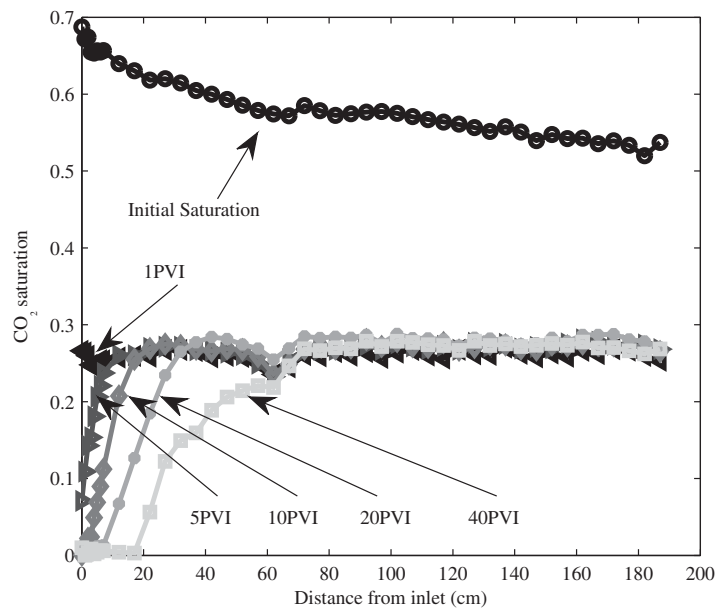
Table 6. Pressure and Temperature Perturbations Required to Account for the Dissolution in of the CO_2

Experiment	Rock Type	Pressure (MPa)	Required Temperature (°C)
Lu et al. [2011]	Tuscaloosa sandstone	10.5	36
Akbarabadi and Piri [2013]	Berea sandstone	2.92	8.92
Akbarabadi and Piri [2013]	Nugget sandstone	2.53	7.82
A, B, C	Berea sandstone	1.05	3

Figure A1. Dissolution dynamics during experiment A, 5M NaCl brine, equilibrated with CO_2 at 14 MPa injected at 10 cm³/min. Circle: initial saturation prior to imbibition. Plots with various gray scale show the saturation profile at 1, 5, 10, 20 and 40 pore volumes of brine injected, respectively.

5. Results showing the dynamics of dissolution for experiment A are reported in Figures A1 and A2. The dissolution front is piston like and the amount of CO_2 dissolved scales linearly with the number of pore volumes of brine injected. This is indicative of a system where the brine is entering the rock core slightly undersaturated with respect to CO_2. The brine quickly becomes saturated, dissolving a small amount of the residually trapped CO_2 in the upstream section of the core and having no further impact on the downstream CO_2 saturation. An important observation from this is that the saturation of CO_2 downstream of the dissolution front remains constant over tens of pore volumes of
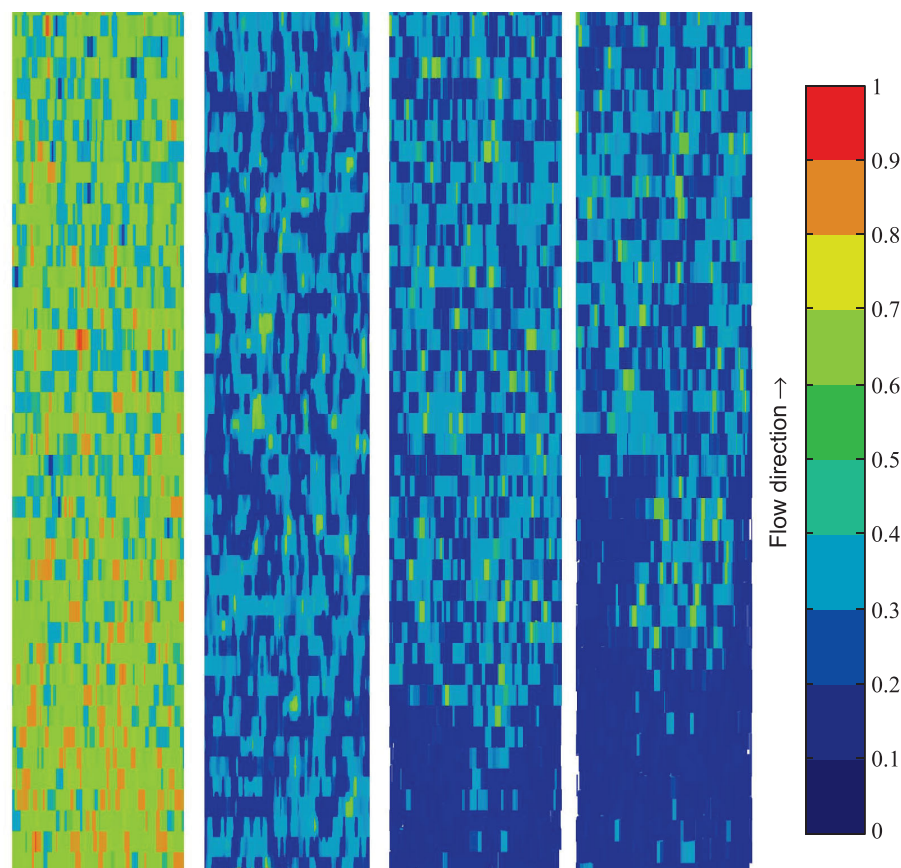

Figure A2. Saturation maps showing CO_2 dissolution in experiment A. From left to right: initial saturation prior to imbibition, saturation at 1PVI, saturation at 10PVI, saturation at 40PVI (the size of the reconstructed images was 142 × 43, with the dimensions of each pixel 250 × 4000 μm).
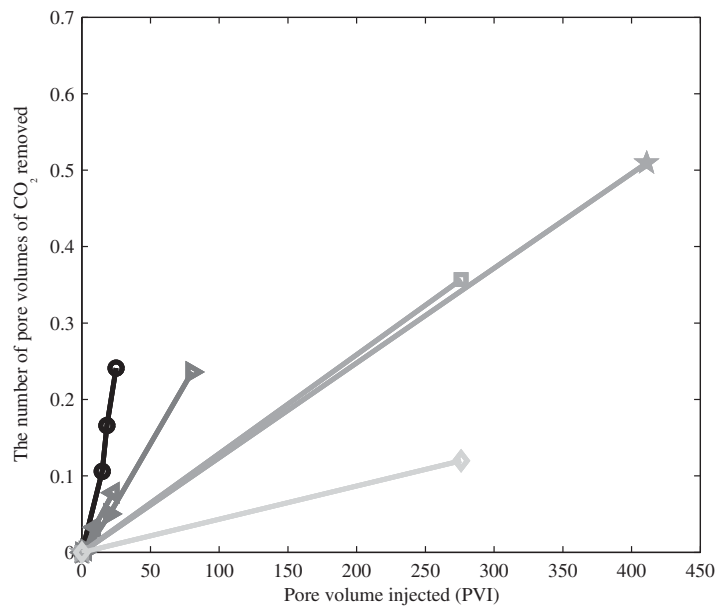
Figure A3. The number of pore volumes of CO_2 removed (i.e., increase in water saturation) plotted against pore volumes of brine injected. Star: Exp. B, square: Exp. C, diamond: dissolution rate with a pressure disequilibrium of 0.35 MPa. Circle: data from *Lu et al.* [2011, Figure 9]. Left-pointing triangle (Berea sandstone) and right-pointing triangle (Nugget sandstone): data from *Akbarabadi and Piri* [2013, Figure 12].

brine injected confirming that was a measure of the stable residually trapped CO_2. Two subsequent tests, Exp. B and Exp. C were performed at higher injection velocity, 20 cm^3/min, to observe the complete dissolution of CO_2 for comparison with other studies. A comparison of the results of all of the experiments with those from other laboratories is shown in Figure A3.

Pressure or temperature disequilibrium are potential sources of the dissolution, including the variation in pressure across the length of the rock core. The level of undersaturation of the CO_2 in the brine entering the core can be estimated from the observed progression of dissolution with the number of pore volumes of

brine injected and this is plotted in Figure A3. A steeper curve is generally indicative of a larger disequilibrium, with some qualification depending on the precise temperature and pressure conditions of the experiment. The required pressure or temperature variation (i.e., brine entering the core that has been equilibrated with CO_2 at a lower pressure or higher temperature) calculated using the solubility model of *Duan and Sun* [2003] is shown in Table 6 and also compared with the other reported studies. In the experimental apparatus used for this work the level of disequilibrium corresponded to an under pressure of 1 MPa or over temperature of 3°C. Pressure variation across the core during the experiments during imbibition was generally far lower than 0.1 MPa and thus it is likely that temperature variation was responsible for the disequilibrium in our system. Additionally, the experimental apparatus appears to perform well as compared with those used in other studies. It was clear from the observations that accurate measures of residual CO_2 could be obtained as long as average saturation values were taken downstream of the dissolution front. This
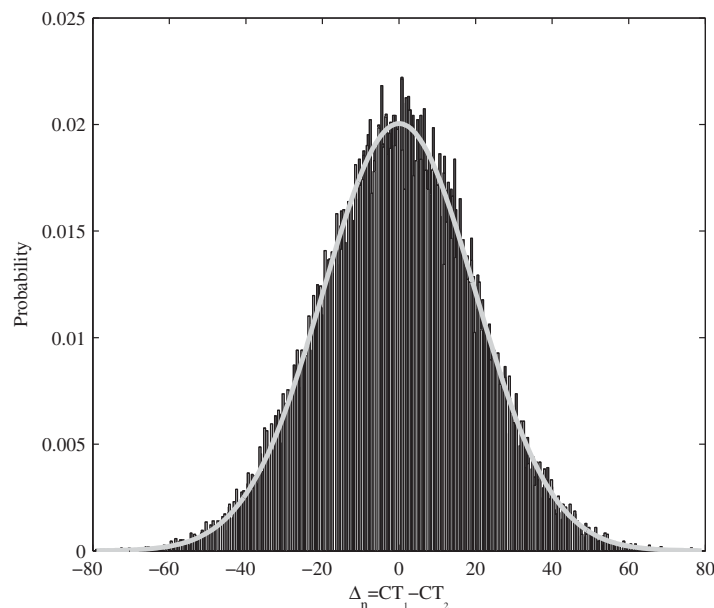

Figure B1. A histogram of CT numbers obtained by taking the difference of two scans of the same location. Various shades of gray represent difference values obtained at various conditions of pressure and temperature but they are indistinguishable indicating that the nature of the noise was intrinsic to the X-ray scanner. From light to dark the histogram bars are taken from: CT images of CO_2 saturated core at 50 bars–50°C, 100 bars–25°C, and 200 bars–50°C, respectively, Gray line: fitted normal distribution curve with mean value $\mu = 0.04$ and standard deviation $\sigma_\triangle = 19.9$.

was straightforward given the slow progression of the dissolution front with the brine injection rates (≤ 0.5 cm^3/min) used in for the residual trapping observations.

Appendix B: Assessment of the Voxel Precision in the CT Imagery

Due to the difference in density contrast between CO_2 and brine at the different test conditions (Table 2) the significance of noise associated with the CT image reconstruction translated into varying degrees of uncertainty in the saturation calculation of individual pixels in the corresponding saturation maps. Noise in the images was random in nature and only dependent on the energy associated with the generation of X-rays, which was the same for all of the tests in this work. Figure B1 shows a characterization of the noise obtained by obtaining the difference between two CT image scans taken at the same conditions and location. The noise had a normal distribution and the uncertainty for the calculated saturation was calculated by the technique described in *Pini et al.* [2012]. In particular, the standard deviation of the saturation, σ_s, was given by

$$\sigma_S = \frac{\sigma_\triangle}{CT_{br} - CT_{CO_2,r}} \sqrt{1 + \left(\frac{CT_{br} - CT_{ex}}{CT_{br} - CT_{CO_2,r}}\right)^2}, \tag{B1}$$

where $\sigma_\triangle$ was the standard deviation of the CT numbers in Hounsfield units of the distribution of values obtained from the difference image. The average uncertainty ranged from 0.115 to 0.379 in saturation units, which was large enough to influence the visual comparison of saturation maps at different conditions of pressure and temperature. Therefore, different coarsening schemes were applied to the images averaging over areas as large as 15×15 voxels such that the uncertainty variance associated with the saturation calculated for a voxel was 0.115–0.129.

References

Akbarabadi, M., and M. Piri (2013), Relative permeability hysteresis and capillary trapping characteristics of supercritical CO_2/brine systems: An experimental study at reservoir conditions, *Adv. Water Resour.*, *52*, 190–206, doi:10.1016/j.advwatres.2012.06.014.

Akin, S., and A. Kovscek (2003), Computed tomography in petroleum engineers research, in *Applications of X-Ray Computed Tomography in the Geosciences*, edited by P. Jacobs and V. Nudde, vol. 215, pp. 23–38, Geol. Soc., London, U. K.

Andrew, M., B. Bijeljic, and M. J. Blunt (2014), Pore-scale imaging of trapped supercritical carbon dioxide in sandstones and carbonates, *Int. J. Greenhouse Gas Control*, *22*, 1–14, doi:10.1016/j.ijggc.2013.12.018.

Bachu, S. (2013), Drainage and imbibition CO_2/brine relative permeability curves at in situ conditions for sandstone formations in western Canada, *Energy Procedia*, *37*, 4428–4436, doi:10.1016/j.egypro.2013.07.001.

Bachu, S., and B. Bennion (2008), Effects of in-situ conditions on relative permeability characteristics of CO_2-brine systems, *Environ. Geol.*, *54*, 1707–1722, doi:10.1007/s00254-007-0946-9.

Berg, S., S. Oedai, and H. Ott (2013), Displacement and mass transfer between saturated and unsaturated CO_2-brine systems in sandstone, *Int. J. Greenhouse Gas Control*, *12*, 478–492, doi:10.1016/j.ijggc.2011.04.005.

Braun, E. M. (2011), *Some practical lessons learned during 30 years in the scal lab, paper SCA2011-01 presented at the International Symposium of the Society of Core Analysts*, Soc. of Core Anal., Austin, Tex.

Broseta, D., N. Tonnet, and V. Shah (2012), Are rocks still water-wet in the presence of dense CO_2 or H_2S?, *Geofluids*, *12*(4), 280–294, doi:10.1111/j.1468-8123.2012.00369.x.

Burnside, N., and M. Naylor (2014), Review and implications of relative permeability of CO_2/brine systems and residual trapping of CO2, *Int. J. Greenhouse Gas Control*, *23*, 1–11, doi:10.1016/j.ijggc.2014.01.013.

Chiquet, P., D. Broseta, and S. Thibeau (2007), Wettability alteration of caprock minerals by carbon dioxide, *Geofluids*, *7*, 112–122, doi:10.1111/j.1468-8123.2007.00168.x.

Doughty, C. (2007), Modeling geological storage of carbon dioxide: Comparison of non-hysteretic and hysterestic characteristic curves, *Energy Convers. Manage.*, *48*(6), 1768–1781, doi:10.1016/j.enconman.2007.01.022.

Duan, Z., and R. Sun (2003), An improved model calculating CO_2 solubility in pure water and aqueous NaCl solutions from 273 to 533 k and from 0 to 2000 bar, *Chem. Geol.*, *193*(3–4), 257–271, doi:10.1016/S0009-2541(02)00263-2.

El-Maghraby, R. M., and M. J. Blunt (2012), Residual CO_2 trapping in Indiana limestone, *Environ. Sci. Technol.*, *47*, 227–233, doi:10.1021/es304166u.

Espinoza, D. N., and J. C. Santamarina (2010), Water-CO_2-mineral systems: Interfacial tension, contact angle, and diffusion—Implications to CO_2 geological storage, *Water Resour. Res.*, *46*, W07537, doi:10.1029/2009WR008634.

Foster, W. (1973), A low-tension waterflooding process, *J. Pet. Technol.*, *25*(2), 205–210, doi:10.2118/3803-PA.

Gammer, D., A. Green, S. Holloway, and G. Smith (2011), The Energy Technologies Institute's UK CO2 storage appraisal project, paper SPE 148426 presented at the SPE Offshore Europe Oil and Gas Conference and Exhibition, Soc. of Pet. Eng., Aberdeen, U. K.

Gershenzon, N. I., M. Soltanian, R. W. Ritzi Jr., and D. F. Dominic (2014), Influence of small scale heterogeneity on CO_2 trapping processes in deep saline aquifers, *Energy Procedia*, *59*, 166–173.

Gupta, S. P., and S. P. Trushenski (1979), Micellar flooding—Compositional effects on oil displacement, *Soc. Pet. Eng. J.*, *19*(02), 116–128, doi:10.2118/7063-PA.

Halland, E. K., I. T. Gjeldvik, W. T. Johansen, C. Magnus, I. M. Meling, S. Pedersen, F. Riis, T. Solbakk, and I. Tappel (2011), CO2 storage atlas Norwegian North Sea, technical report, Norwegian Pet. Dir, Stavanger, Norway.

Hesse, M., F. O. Jr., and H. Tchelepi (2008), Gravity currents with residual trapping, *J. Fluid Mech.*, *611*, 35–60, doi:10.1017/S002211200800219X.

Iglauer, S., A. Paluszny, C. H. Pentland, and M. J. Blunt (2011), Residual CO_2 imaged with X-ray micro-tomography, *Geophys. Res. Lett.*, *38*, L21403, doi:10.1029/2011GL049680.

Jerauld, G. (1997), Prudhoe bay gas/oil relative permeability, *SPE Reservoir Eng.*, *12*(1), 66–73, doi:10.2118/35718-PA.

Joekar-Niasar, V., F. Doster, R. Armstrong, D. Wildenschild, and M. Celia (2013), Trapping and hysteresis in two-phase flow in porous media: A pore-network study, *Water Resour. Res.*, *49*, 4244–4256, doi:10.1002/wrcr.20313.

Juanes, R., E. Spiteri, F. M. Orr Jr., and M. Blunt (2006), Impact of relative permeability hysteresis on geological CO_2 storage, *Water Resour. Res.*, *42*, W12418, doi:10.1029/2005WR004806.

Jung, J.-W., and J. Wan (2012), Supercritical CO_2 and ionic strength effects on wettability of silica surfaces: Equilibrium contact angle measurements, *Energy Fuels*, *26*, 6053–6059, doi:10.1021/ef300913t.

Killough, J. (1976), Reservoir simulation with history-dependent saturation functions, *Soc. Pet. Eng. J.*, *16*(1), 37–48, doi:10.2118/5106-PA.

Kleppe, J., P. Delaplace, R. Lenormand, G. Hamon, and E. Chaput (1997), Representation of capillary pressure hysteresis in reservoir simulation, paper SPE 38899 presented at the SPE Annual Technical Conference and Exhibition, Soc. of Pet. Eng., San Antonio, Tex.

Krevor, S. C. M., R. Pini, B. Li, and S. M. Benson (2011), Capillary heterogeneity trapping of CO_2 in a sandstone rock at reservoir conditions, *Geophys. Res. Lett.*, *38*, L15401, doi:10.1029/2011GL048239.

Krevor, S. C. M., R. Pini, L. Zuo, and S. M. Benson (2012), Relative permeability and trapping of CO_2 and water in sandstone rocks at reservoir conditions, *Water Resour. Res.*, *48*, W02532, doi:10.1029/2011WR010859.

Kumar, A., R. Ozah, M. Noh, G. Pope, S. Bryant, K. Sepehrnoori, and L. Lake (2005), Reservoir simulation of CO_2 storage in deep saline aquifers, *SPE J.*, *10*(3), 336–348, doi:10.2118/89343-PA.

Kuo, C.-W., J.-C. Perrin, and S. M. Benson (2010), Effect of gravity, flow rate, and small scale heterogeneity on multiphase flow of CO_2 and brine, paper SPE 132607 presented at the SPE Western Regional Meeting, Soc. of Pet. Eng., Anaheim, Calif.

Lake, L. W. (1989), *Enhanced Oil Recovery*, Prentice Hall, Upper Saddle River, N. J.

Land, C. S. (1968), Calculation of imbibition relative permeability for two- and three-phase flow from rock properties, *Soc. Pet. Eng. J.*, *8*(2), 149–156, doi:10.2118/1942-PA.

Lenhard, R., and J. Parker (1987), A model for hysteretic constitutive relations governing multiphase flow, *Water Resour. Res.*, *23*(12), 2197–2206, doi:10.1029/WR023i012p02197.

Li, B., and S. M. Benson (2014), Small-scale heterogeneities and buoyancy-drive CO_2 migration in geological storage, *Energy Procedia*, *68*, 3608–3615, doi:10.1016/j.egypro.2014.11.391.

Li, K. (2004), *Theoretical development of the Brooks-Corey capillary pressure model from fractal modelling of porous media, paper SPE 89429 presented at the SPE/DOE Symposium on Improved Oil Recovery*, Soc. of Pet. Eng., Tulsa, Okla.

Lu, J., K. Milliken, R. M. Reed, and S. Hovorka (2011), Diagenesis and sealing capacity of the middle Tuscaloosa mudstone at the Cranfield carbon dioxide injection site, Mississippi, USA, *Environ. Geosci.*, *18*(1), 35–53, doi:10.1306/eg.09091010015.

Ma, T., and T. Youngren (1994), Performance of immiscible water-alternating-gas (IWAG) injection at Kuparuk river unit, north slope Alaska, paper SPE-28602-MS presented at the SPE Annual Technical Conference and Exhibition, Soc. of Pet. Eng., New Orleans, La.

Naar, J., and J. Henderson (1961), An imbibition model—Its application to flow behavior and the prediction of oil recovery, *Soc. Pet. Eng. J.*, *1*(2), 61–70, doi:10.2118/1550-G.

Oak, M. J., L. E. Baker, and D. C. Thomas (1990), Three-phase relative permeability of Berea sandstone, *J. Pet. Technol.*, *42*(08), 1054–1061, doi:10.2118/17370-PA.

Pentland, C. H., E. Itsekiri, S. K. A. Mansoori, S. Iglauer, B. Bijeljic, and M. J. Blunt (2010), Measurement of nonwetting-phase trapping in sandpacks, *SPE J.*, *15*(2), 274–281, doi:10.2118/115697-PA.

Pentland, C. H., R. El-Maghraby, S. Iglauer, and M. J. Blunt (2011), Measurements of the capillary trapping of super-critical carbon dioxide in Berea sandstone, *Geophys. Res. Lett.*, *38*, L06401, doi:10.1029/2011GL046683.

Pini, R., S. C. Krevor, and S. M. Benson (2012), Capillary pressure and heterogeneity for the CO_2/water system in sandstone rocks at reservoir conditions, *Adv. Water Resour.*, *38*, 48–59, doi:10.1016/j.advwatres.2011.12.007.

Qi, R., T. LaForce, and M. J. Blunt (2009), Design of carbon dioxide storage in aquifers, *Int. J. Greenhouse Gas Control*, *3*(2), 195–205, doi:10.1016/j.ijggc.2008.08.004.

Richardson, J., J. Kervor, J. Hafford, and J. Osoba (1952), Laboratory determination of relative permeability, *J. Pet. Technol.*, *4*(8), 187–196, doi:10.2118/952187-G.

Saadatpoor, E., S. L. Bryant, and K. Sepehrnoori (2010), New trapping mechanism in carbon sequestration, *Transp. Porous Media*, *82*(1), 3–17, doi:10.1007/s11242-009-9446-6.

Salathiel, R. (1973), Oil recovery by surface film drainage in mixed-wettability rocks, *J. Pet. Technol.*, *25*(10), 1216–1224, doi:10.2118/4104-PA.

Silin, D., L. Tomutsa, S. M. Benson, and T. W. Patzek (2011), Microtomography and pore-scale modeling of two-phase fluid distribution, *Transp. Porous Media*, *86*, 495–515, doi:10.1007/s11242-010-9636-2.

Spiteri, E. J., R. Juanes, M. J. Blunt, and F. M. Orr Jr. (2008), A new model of trapping and relative permeability hysteresis for all wettability characteristics, *SPE J.*, *13*(3), 277–288, doi:10.2118/96448-PA.

Suekane, T., S. H. T. Nobuso, and M. Kiyota (2008), Geological storage of carbon dioxide by residual gas and solubility trapping, *Int. J. Greenhouse Gas Control*, *2*, 58–64, doi:10.1016/S1750-5836(07)00096-5.

Taber, J. (1969), Dynamic and static forces required to remove a discontinuous oil phase from porous media containing both oil and water, *SPE J.*, *9*(1), 3–12, doi:10.2118/2098-PA.

Wang, F. (1988), Effect of wettability alteration on water/oil relative permeability, dispersion, and flowable saturation in porous media, *SPE Reservoir Eng.*, *3*(2), 617–628, doi:10.2118/15019-PA.

Warwick, P. D., et al. (2013), National assessment of geologic carbon dioxide storage resources—Results, *U.S. Geol. Surv. Circ.*, 12–16.

Wiebe, R. (1941), The binary system carbon dioxide-water under pressure, *Chem. Rev.*, *29*(3), 475–481, doi:10.1021/cr60094a004.

Wiebe, R., V. L. Gaddy, and C. Heins (1933), The solubility of nitrogen in water at 50, 75 and 100°C from 25 to 1000 atmospheres, *J. Am. Chem. Soc.*, *55*(3), 947–953, doi:10.1021/ja01330a011.